EXPERIMENTAL STUDIES AND CFD CALCULATIONS FOR BUOYANCY DRIVEN MIXING PHENOMENA

Marco Jose da Silva, Sebastian Thiele, Thomas Höhne, Roman Vaibar, Uwe Hampel

Institute of Safety Research, Forschungszentrum Dresden-Rossendorf e.V., Dresden, Germany

Abstract

Buoyancy driven flow is found in many engineering application such as the mixing of fluids with different densities. In nuclear reactor safety the mixing of borated and deborated water is a critical issue that needs investigation, assessment and prediction. As nuclear reactor geometries are complex, in this study a simple vertical mixing test facility (VeMix) was used to validate numerical models. Through the application of defined initial conditions in the test facility the mixing process could also be predicted by CFD simulations performed with ANSYS CFX software. A newly developed planar sensor was applied to experimentally investigate the mixing process. The sensor yields images of fluid distribution over the sensor's surface by individually interrogating the conductivity of a multitude of sensing structures. Furthermore, an image processing algorithm based on the optical flow concept was implemented and tested which allows the measurement of flow pattern velocities. Validation experiments were performed in the VeMix test facility which show typical vertical and horizontal flow pattern under different flow regimes. The data from the planar sensor of mixing process and velocity fields were used for the validation of the simulation results. Comparisons of the experimental results with the corresponding simulations show similar flow patterns and typical periodic behavior.

1. INTRODUCTION

Buoyancy driven flow is often found in many engineering application such as mixing process of fluids with different density. In nuclear reactors, fluid mixing induced by buoyancy effect is relevant for

- boron dilution issues, when highly borated water with different temperature mixes with the ambient water in the reactor pressure vessel,
- pressurized thermal shock scenarios, when cold emergency cooling water is injected into the reactor and is contacted with the vessel wall, and
- containment analysis, when in the case of severe accidents, hot hydrogen and steam mix with the containment atmosphere.

Especially the problems related to the fluid mixing of borated and unborated water has been the scope of investigation (Rohde et al., 2005; Höhne et al., 2006). In certain situations such as when a lack of boron concentration occurs in the reactor, additional borated water is added to the core via an emergency injection system. This borated water has usually a colder temperature than the ambient coolant. Therefore, both the boron concentration and the temperature will affect the density difference of the fluids being mixed and therefore affect the mixing processes that occur in such situations. Thus, the degree of mixing of weakly and highly borated coolant is a critical issue with respect to the reactivity insertion into the reactor core. In this way, understanding the impact of such phenomena can help in the design and operation of nuclear reactors and many other process industry operations.

The aim of the present study is to analyze the mixing processes related to the boron dilution problem in reactor safety-relevant scenarios. A combined numerical and experimental study of buoyant mixing processes has been performed. A simple vertical test facility called VeMix was chosen for validation of numerical models of the mixing process, as nuclear reactor geometries are complex leading to the mixing processes that are not widely understood or where the influence of the buoyancy may not be significant.

In the following section, the experimental test facility VeMix, the CFD models used and typical flow regimes encountered are described. A newly developed planar sensor along with optical observations was applied for the experimental evaluation of buoyancy driven flows. The use of the optical flow method allows the estimation of velocity fields of the experimental data obtained with the planar sensor. The planar sensor as well as the working principle and implementation of data processing algorithm based on the optical flow method are described in section 3. Finally, the experimental and simulation results are presented and discussed in section 4.

2. EXPERIMENTAL SETUP AND CFD MODEL

2.1. VeMix test facility

A vertical mixing test facility (VeMix) with simple geometry having rectangular cross section was designed and constructed (Fig. 1). Five identical rectangular segments are stacked together. Each segment is made of acrylic glass which is 500 mm wide by 625 mm high by 100 mm deep. The whole test section is 3.32 m high. A flow inlet is located in between segments 1 and 2, while an outlet is positioned in between segments 4 and 5. Segment number 2, right after the inlet, is instrumented with the planar sensor (see section 3). In this region the most interesting mixing process occurs. The facility ensures that the gravity force acts along a significant length scale.

In order to visualize the mixing process of two liquids having different densities in a controlled manner, the following experiment was carried out. Water-glucose mixtures were used to produce density gradients. A glucose-water solution containing 6% glucose has a corresponding density of 1020 $kg \cdot m^{-3}$, i.e. 2% density difference to distilled water.

The execution of one single experiment consists of few subsequent steps.

1. Water is added into the test section up to the bottom of segment 2.
2. Water-glucose solution is very slowly inserted from the bottom taking care not to mix both components. In this way, a layered structured is obtained having clean water in segments 1-2 and the more dense water-glucose solution in segments 3-5. This step ensures the formation of a well-defined initial condition which is very important for later comparison purposes with CFD simulations.
3. Finally, the mixing process is initiated by flowing water-glucose solution through the inlet with a given constant flow rate.

2.2. CFD model

The CFD code for simulating the mixing studies was CFX-11 (CFX11, 2007). CFX-11 is an element-based finite-volume method with second-order discretisation schemes in space and time. It uses a coupled algebraic multigrid algorithm to solve the linear systems arising from discretisation. The discretisation schemes and the multigrid solver are scalably parallelized. CFX-11 works with unstructured hybrid grids consisting of tetrahedral, hexahedral, prism and pyramid elements. An extensive grid study was done and as a result of it, a uniform hexahedral node distribution was selected for the simulations, whereby the resulting grid has 420,000 nodes and 346,000 elements.

The following parameters were used in the simulations discussed in this section. The SST buoyancy turbulence model was used. The SST model (Menter, 2002) works by solving a turbulence/frequency-based model ($k–\omega$) at the wall and $k-\varepsilon$ in the bulk flow. A blending function ensures a smooth transition between the two models.

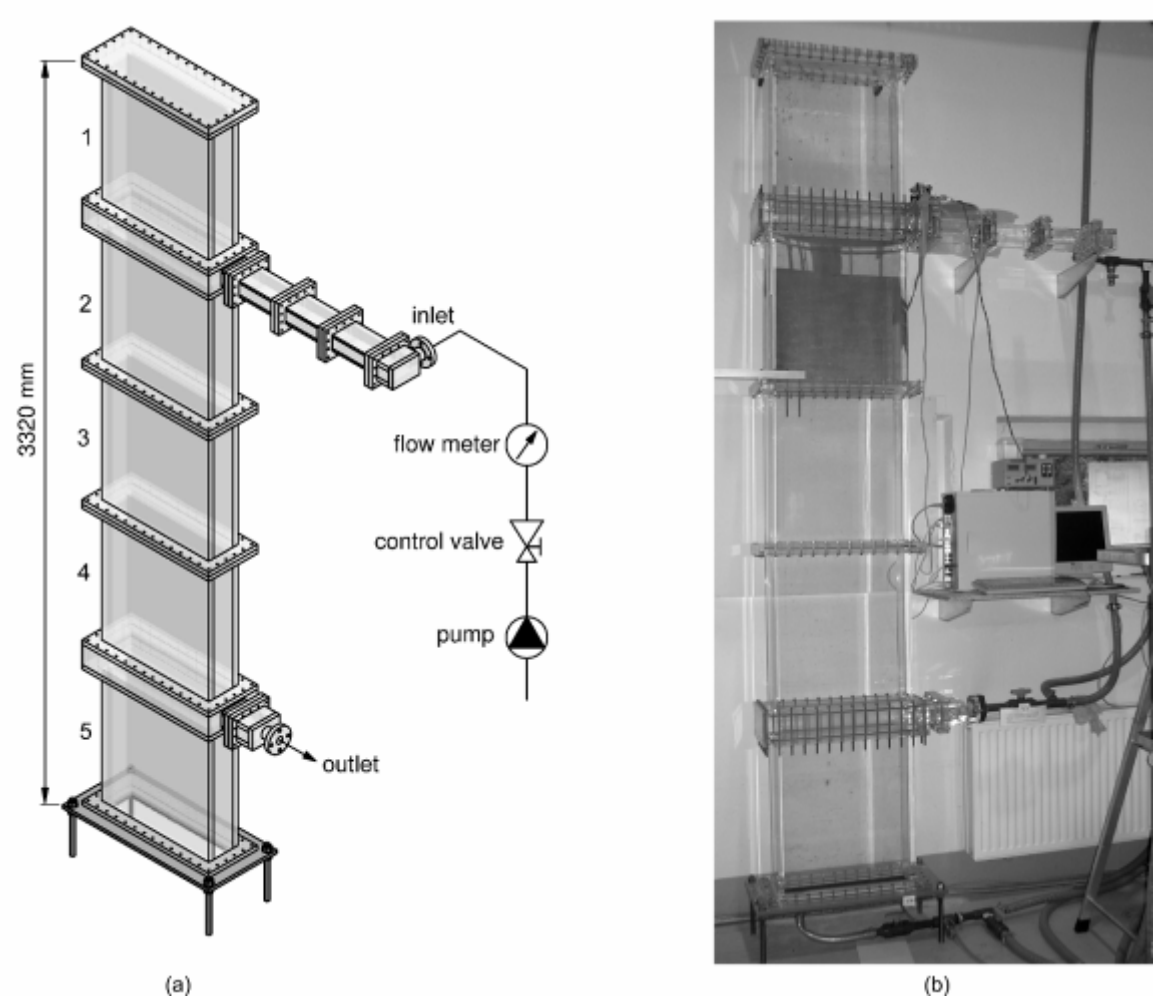

Fig. 1: Schematic diagram (a) and photograph (b) of the test facility used in the buoyancy-driven flow experiment.

All transient calculations were done with the higher order scheme "High Resolution" in space and "Fully implicit 2nd order backward Euler" in time. For both discretization schemes the target variable does not change any more for convergence criteria below 1×10^{-4}. Therefore this convergence criterion is used for all calculations. Double precision was used. The inlet boundary conditions were set depending on the chosen flow rate, i.e.

- velocityIn = Q / A
- velocityOut = Q / A

where Q is the flow rate and A = 0.05 m^2 the cross-section area of the VeMix test section. Furthermore, for all simulations and experiments water with ρ_w = 997 kg/m^3 (T = 25 °C) and water-glucose solution with a density of ρ_{wgs} = 1017 kg/m^3 were used, i.e. with a density gradient of $\Delta\rho$ = 2%.

The domain was filled up to 1.8 m, i.e. up to bottom of segment 2, with heavy liquid. Transient experimental values were used. No specific velocity profile is given. As an initial guess of the turbulent kinetic energy and the dissipation rate the code standard is used. The outlet boundary condition was an opening using outflow velocities. The multicomponent buoyant flow option using different fluid densities were used to describe the mixing processes (Höhne, 2006).

Transient calculations with 300 s simulation time with time steps

- Δt = 0.1 s, for $0 \le t \le 30$, and
- Δt = 0.5 s for $30 < t \le 300$

were performed on the FZD LINUX cluster. The cluster runs at Linux Scientific 64 bit operational system and comprises 32 AMD OPTERON Computer Nodes. Each computer node is formed by 2 × AMD OPTERON 285 (2.6 GHz, dual-core) with 16 GB memory. Simulations took approximately 3 days each to complete. Four processors were used for the simulations presented here in a parallel mode with the message passing protocol PVM.

2.3. Flow characterization

Through the application of defined initial conditions as described above the mixing process could also be investigated by CFD simulations. First validations of the simulated flow were performed by visual inspection of mixing behavior by a video camera. For this purpose, water-glucose solution was marked with a blue dye tracer. Fig. 2 shows snap shots of simulation results and images taken with the camera for the indicated conditions which show typical vertical and horizontal flow pattern under different flow regimes.

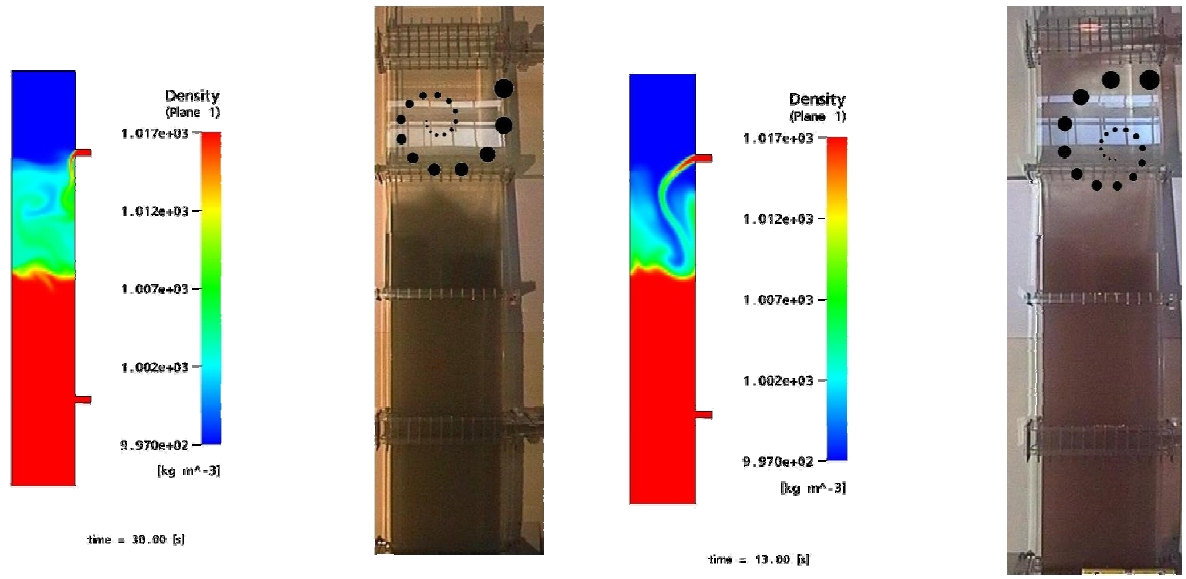

(a) falling down regime: flow rate = 0.4 l/s, Ri = 2.12 (b) horizontal jet regime: flow rate = 0.7 l/s, Ri = 0.69

Fig. 2: Flow regime during the flow condition Δρ = 2%, L = 0.83 m and flow rate is indicated in each figure. The water-glucose solution was marked with a dye tracer.

The observed flow behavior can be characterized by an internal Richardson number, a non-dimensional number which is the ratio between the buoyancy and the momentum forces

$$Ri = \frac{g \cdot L^2 \cdot \Delta\rho}{\rho_w \cdot v^2} \tag{1}$$

where g = 9.81 m/s^2 is the acceleration due to gravity, L characteristic length scale, which defines the thickness of the layer between the clean water and water-glucose solution $L = H_{inlet} - H_{fill}$, H_{inlet} = 2.63 m and H_{fill} = 1.8 m for the case here, $\Delta\rho$ density difference between the two liquids, ρ_w clean water density and v the characteristic velocity of the VeMix test facility, which describes the movement of the interface between the liquids and is determined by

$$v = \frac{Q}{A}. \tag{2}$$

where Q is the flow rate and A = 0.05 m^2 the cross-section area of the VeMix test section. Other characteristic length and velocity scales could be applied in definition of the Richardson number, for instance, the hydraulic inlet area in (2) for the definition of the characteristic velocity. However the described scales were chosen because they enhance the sensitivity of the obtained Richardson numbers regarding to the flow pattern transition of regimes and thus better describe the mixing pattern developed in the facility.

Basically two different flow regimes can be indentified from the simulation and experiments and are properly characterized by the Richardson number:

- for $Ri > 2$ regime of flow falling jet patterns are shown in fig. 2a . The gravity force acts along the vertical axis and is significantly stronger than momentum forces driven by inlet flow rate. The jet drops near to the wall below the inlet nozzle.
- for $Ri < 1$ regime of flow horizontal jet patterns are shown in fig. 2b. The momentum force driven by input flow rate is stronger than gravity force, which results in the formation of a horizontal jet. The horizontal jet influences the transient mixing behavior, as oscillation waves are formed on interface between the heavier water and the lighter water.

For intermediate values between 1 and 2 a transition regime occurs. The gravity and momentum forces are in near equilibrium and the resulting flow pattern strongly depends on the force ratio. In this regime it is not easy to predict the flow pattern observed.

3. PLANAR ARRAY SENSOR AND VELOCITY FIELD ESTIMATION

3.1. Planar array sensor

The most interesting location in the VeMix vessel was found to be just below the inlet nozzle. Therefore, the planar sensor was placed here in order to study the mixing behavior of the two liquids. The planar array sensor used to investigate the mixing behavior was manufactured using standard printed-circuit board (PCB) fabrication technology. It was built in a rectangular geometry with 4096 interdigital sensing structures evenly distributed over an area of 620 mm × 500 mm (figure 3). The interdigital sensing structures are multiplexed in a matrix with 64 driver (rows) and 64 sensing electrodes (columns). The sensor board was designed to fit to a segment of the VeMix experimental flow channel (see section 2).

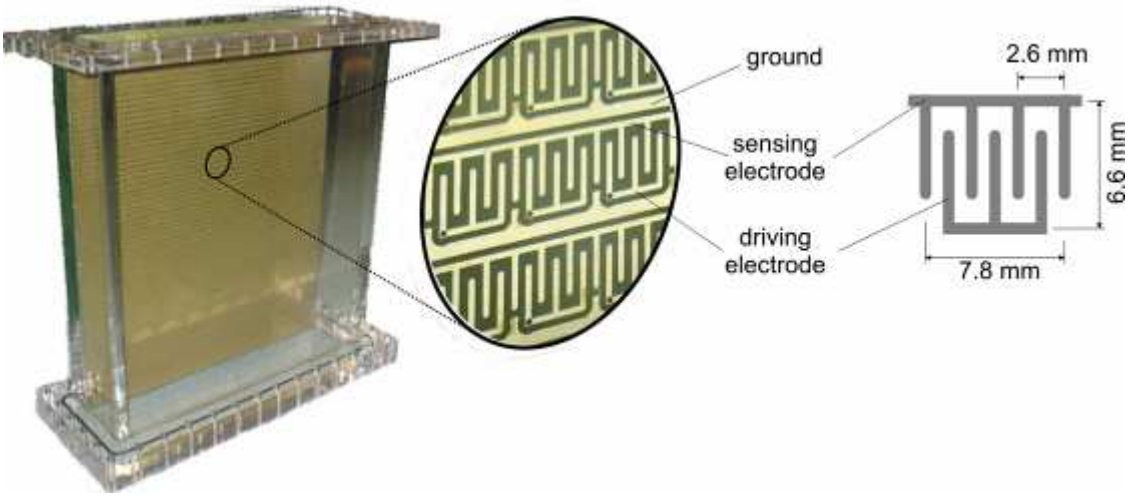

Fig. 3: Printed-circuit board of a planar sensor containing 64 × 64 interdigital sensing structures fitted to a segment of VeMix test facility. The size of each sensing structure is 5.8 mm × 6.6 mm and the size of the whole sensor is 620 mm by 500 mm.

An associated electronics measures the liquid conductivity of each sensing structures in a multiplexed and fast manner. The transmitter electrodes are sequentially excited by a bipolar voltage signal while the non-active electrodes are grounded. The electrical currents flowing from the activated transmitter electrode to the receiver electrodes are measured synchronously while the transmitter electrodes are being activated consecutively. After all transmitter electrodes have been activated once a complete frame of the conductivity distribution at all sensor structures has been acquired. Figure 4 depicts a schematic diagram of the electronics and the timing diagram of the electrical signals. The maximal frame rate achievable for this sensor is 2,500 images/s (Da Silva et al., 2007).

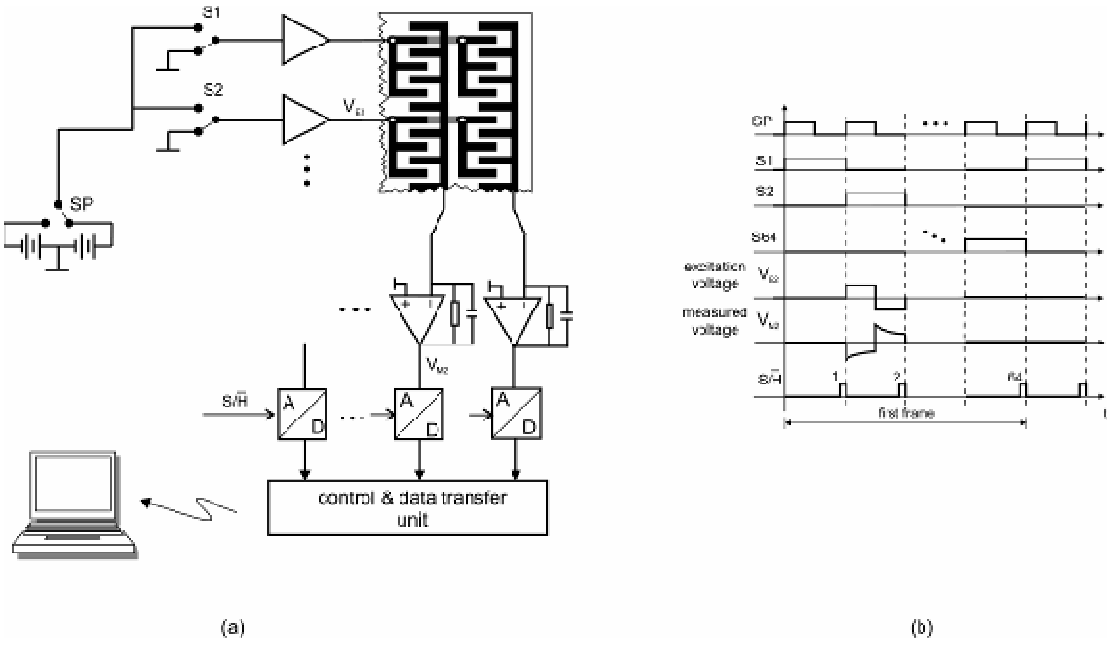

Fig. 4: (a) Simplified block diagram of the measuring electronics. (b) Timing diagram for the multiplexed excitation and measuring scheme for the sensor. Voltages are sampled at the rising edge of the sample-and-hold signal. One frame is complete when the 64 transmitter electrodes have been activated and all currents have been measured. The signal SP denotes the polarity switch and S1 to S64 the analog switches.

Basically, the voltage values measured by the surface sensor are proportional to the electrical current flowing from transmitter electrodes to receiver electrodes. This current in turn depends on the electrical conductivity κ of the operating liquid and on the liquid wetting level of a sensing structure. Since the liquid level over the sensor is always constant in the VeMix test facility, it can be stated that the measured voltage is directly proportional to the liquid conductivity value of each sensing structure in the form (Da Silva et al., 2007):

$$V(i,j,k) = \kappa \cdot a(i,j) + b(i,j), \tag{3}$$

where V is the electronics' voltage output, a and b are constants, and i and j denote spatial coordinates and k the temporal point index. As described in detail in section 2, to simulate density gradients clean water and water-glucose mixtures were used as fluids in the present work. Additionally, one of the fluids was marked with a NaCl salt tracer to introduce conductivity differences and thus making the mixing process of clean water and glucose-water solution visible to the planar sensor. It has been shown that the conductivity measurement can be linked to density gradients by (Prasser et al., 2003)

$$\Theta(i,j,k) = \frac{V(i,j,k) - V_{\mathrm{L}}}{V_{\mathrm{H}} - V_{\mathrm{L}}} = \frac{\kappa(i,j,k) - \kappa_{\mathrm{L}}}{\kappa_{\mathrm{H}} - \kappa_{\mathrm{L}}} \cong \frac{\rho(i,j,k) - \rho_{\mathrm{L}}}{\rho_{\mathrm{H}} - \rho_{\mathrm{L}}} \tag{4}$$

where Θ is called mixing scalar (assuming values between 0 and 1), V is the measured voltage, κ conductivity, and ρ density. The subscripts H and L stand for the high and low values, respectively, which represent the parameter difference of the used liquids.

3.2. Optical flow

Computation of velocity distribution from measured image data gained increasing attention since improved performance of computers enabled calculation of computationally intensive codes. Up to now numerous image processing modalities of optical flow techniques have been proposed for motion estimation which present some advantages over cross-correlation methods (Beauchemin and Barron, 1995; Jähne, 2002; Corpetti et al., 2004). These methods have been developed especially for processing of images from optical acquisition systems. There, the projected motion field from the real 3D-scene onto the image scene is extracted from the spatio-temporal change of the gray values in the corresponding image sequence which is defined as optical flow (Jähne, 2002). The optical flow method evaluates the change of brightness (or intensity) in a sequence of images caused, for example, by the movement of an object, and corresponds these intensity gradients to a velocity field.

The planar array sensor is evidently no optical acquisition system and the gray values in the images represent an electrical parameter, i.e. the measured conductivity value at each electrode pair is represented by a gray value of the corresponding pixel in the image. However, the measured 2D conductivity value distribution represents the projected flow scene on the sensor surface in a given experiment and thus carries information of the superficial velocity field. That is, the velocity field can be calculated from the gradients of the gray values. The velocity vector $\boldsymbol{v}(x,y)$ can be inferred from the 2D optical flow vector by the relation

$$\boldsymbol{v}(x,y) = \frac{k_\mathrm{g}}{\Delta t} \cdot \boldsymbol{f}(i,j) = \begin{pmatrix} f_\mathrm{i} \\ f_\mathrm{j} \end{pmatrix}, \tag{5}$$

where k_g is an scalar value which describes the geometry factor of the system and Δt is the time between two consecutive images.

3.3. Optical flow for the planar sensor data

As a first step, we implemented a differential optical flow algorithm to estimate the flow vector $\boldsymbol{f}(i,j)$ for each pixel i and j at time t of the 2D-image from the spatio-temporal derivatives of the gray values in the image sequence. For the present sensor, i and j vary from 1 to 64, since the sensor has 64 × 64 sensing structures. The algorithm is based on a concept similar to the continuity equation in fluid dynamics, where the amount of mass is constant. Here the gray value distribution $g(i,j)$ in local time-varying image areas is assumed to be nearly constant for a short period, which yields the optical flow constraint equation

$$\nabla g \cdot \boldsymbol{f} + g_t = 0, \tag{6}$$

where ∇g is the local gradient of gray value, i.e. the spatial derivatives of the local gray value

$$\nabla g = \begin{pmatrix} \dfrac{\partial g}{\partial x} \\ \dfrac{\partial g}{\partial y} \end{pmatrix} \approx \begin{pmatrix} \dfrac{\Delta g}{\Delta x} \\ \dfrac{\Delta g}{\Delta y} \end{pmatrix} = \begin{pmatrix} g_i \\ g_j \end{pmatrix} \tag{7}$$

in horizontal direction x and vertical direction y corresponding to the indices i and j in the image plane (Jähne, 2002). Further, g_t is the discrete temporal derivative of the local gray value

$$\frac{\partial g}{\partial t} \approx \frac{\Delta g}{\Delta t} = g_t \,. \tag{8}$$

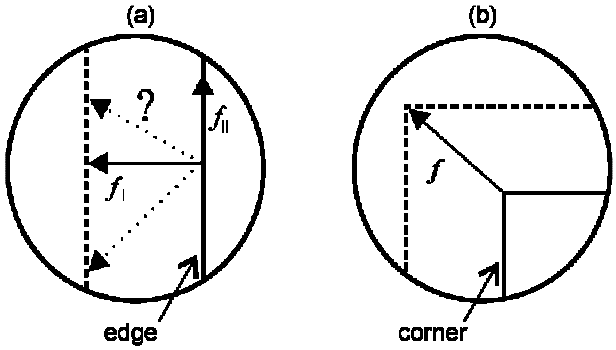

Figure 5: Illustration of the local view to the image through the spatio-temporal derivatives. The displacement vector of the edge in a) can not be determined exactly due to the aperture problem, whereas the movement of the corner b) can be observed correctly.

However, the spatio-temporal derivatives are local operators, which act only in small regions of the image, which can be illustrated as a mask or aperture applied to the image (see fig. 5). The solid line in fig. 5a corresponds to an edge that is moving to the position of the dashed line in the second image. Due to the limited view of the local operators, the displacement vector of the optical flow may be connected from one point on the solid line to any point on the dashed line, i.e. there is no unambiguous correspondence. Thus, only the normal component $f_{\perp}$ of the displacement vector can be correctly determined, whereas the parallel $f_{\parallel}$ component remains unknown. This phenomenon is well known as aperture problem (Jähne, 2002). Thus, the optical flow constraint equation (6) is ill-posed. With the local operators the vector can only be determined exactly when a corner of the object falls within the mask of the local operators as depicted in fig. 5b.

Due to the aperture problem, further conditions have to be taken into account to determine the vector of the optical flow. We used a global smoothness constraint first introduced by Horn and Schunk (1981) for regularization of the optical flow constraint equation. The global smoothness constraint assumes that optical flow vectors of neighboring pixels are nearly identical, i.e. the difference between the local average value of the optical flow $\overline{\boldsymbol{f}}$ and the optical flow of the neighboring pixels is assumed to be minimal. This hypothesis yields the quadratic difference

$$\delta_f^2 = \left(\overline{\boldsymbol{f}} - \boldsymbol{f}\right)^2 . \tag{9}$$

Combining equation (9) with the uncertainty in the constraint equation resulting from signal noise

$$\delta_n = \nabla g \cdot \boldsymbol{f} + g_t \tag{10}$$

yields the overall uncertainty constraint

$$\delta^2 = \alpha^2 \cdot \delta_f^2 + \delta_n^2 \,, \tag{11}$$

which has to be minimized to achieve an estimation of the optical flow vector field, where α is a fixed weighting factor being estimated empirically, to adjust the impact of both terms of the uncertainty. In our calculations the value of 0.1 was used. Minimization of δ^2 is achieved by claiming

$$\frac{\partial \delta^2}{\partial f_\mathrm{i}} \stackrel{!}{=} 0 \tag{12}$$

and

$$\frac{\partial \delta^2}{\partial f_\mathrm{j}} \stackrel{!}{=} 0\,, \tag{13}$$

from which one obtains two equations to be solved for each individual component of $\boldsymbol{f}$. Since analytical solution of these both equations for all pixels of the image is highly computational intensive, an iterative set of two equations is derived from (12) and (13) according to the Gauss-Seidel method (Horn and Schunk, 1981):

$$f_\mathrm{i}^{\mathrm{n+1}} = \bar{f}_\mathrm{i}^{\mathrm{n}} - g_\mathrm{i} \frac{g_\mathrm{i} \cdot \bar{f}_\mathrm{i}^{\mathrm{n}} + g_\mathrm{j} \cdot \bar{f}_\mathrm{j}^{\mathrm{n}} + g_\mathrm{t}}{\alpha^2 + g_\mathrm{i} + g_\mathrm{j}} \tag{14}$$

and

$$f_\mathrm{j}^{\mathrm{n+1}} = \bar{f}_\mathrm{j}^{\mathrm{n}} - g_\mathrm{j} \frac{g_\mathrm{i} \cdot \bar{f}_\mathrm{i}^{\mathrm{n}} + g_\mathrm{j} \cdot \bar{f}_\mathrm{j}^{\mathrm{n}} + g_\mathrm{t}}{\alpha^2 + g_\mathrm{i} + g_\mathrm{j}}\,. \tag{15}$$

Equations (14) and (15) are solved iteratively for every step in time t and the optical flow in the iteration $(n + 1)$ is estimated by the spatio-temporal derivatives and the previous locally averaged optical flow $\bar{\boldsymbol{f}}^{\mathrm{n}}$ (Horn and Schunk, 1981). The iterative algorithm for every step in time t is shortly described below. Initially, the spatio-temporal derivatives are calculated for every pixel and the averaged values $\bar{f}_\mathrm{i}^{0}$ and $\bar{f}_\mathrm{j}^{0}$ are set to zero. The first iteration is carried out yielding the optical flow components f_i^{1} and f_j^{1}. The neighboring pixels are averaged locally with a 2D-averaging filter for every pixel of the image to achieve $\bar{f}_\mathrm{i}^{1}$ and $\bar{f}_\mathrm{j}^{1}$ which are used in the next iteration. This process is repeated until the difference between two iterations is below a given value in the form

$$\left| \boldsymbol{f}^{\mathrm{n+1}} - \boldsymbol{f}^{\mathrm{n}} \right| \leq \varepsilon\,, \tag{16}$$

which is the norm of the difference between two consecutive iterations. In the calculations we empirically chose ε to be 10^{-3}. In this way, the progress of the algorithm is adapted to the individual composition of the local spatio-temporal derivatives.

In fact, the calculation of the local spatio-temporal derivatives in the standard algorithm by Horn and Schunk (1981) achieves sufficient accuracy in case of linear gray value distributions and oversampled image data only (Beauchemin and Barron, 1995). To achieve improved performance of the algorithm we implemented a method that evaluates five consecutive images for estimation of spatio-temporal derivatives for each step in time t, which are then applied in the iterative calculation of the current optical flow vector field according to (14) and (15) (Simoncelli, 1994; Thiele, 2007). Once the optical flow is calculated the velocity can be easily achieved by implying the spatial dimensions of the sensing elements and the data acquisition rate, as described in eq. (5).

4. COMPARISONS: EXPERIMENT AND SIMULATION

In this section, the experimental and simulation results for an exemplary flow condition are presented. Following parameters were used: flow rate Q = 0.35 l/s, H_{fill} = 2.12 m (i.e. L = 0.51 m), $\Delta\rho$ = 2%. In this fashion, the Richardson number calculated from eq. (1) is 0.882 and as described in section 2.3 the horizontal jet pattern flow regime is predicted.

Simulations were performed with the CFD model explained in section 2.2. The planar array sensor was set to acquire 200 images per second during 100 s. In the experiment, clean water ρ_w = 997 kg/m^3 and water-glucose solution ρ_{wgs} = 1017 kg/m^3 having a conductivity of 60 µS/cm and 200 µS/cm, respectively, were used. The velocity fields were computed by the optical flow method as presented in section 3.3.

4.1. Fluid distribution

In fig. 6 images of the distribution of mixing scalar Θ (eq. (4)) from the measured and simulated results are depicted. It is very clear to see the formation of a circular jet, as the water-glucose solution flows into the channel from both experiment and simulation. It seems that in the experiment the substances get mixed more rapidly and therefore the jet is more pronounced in the simulated distributions. In the experiment, a transition layer at the bottom of the images can be observed. It is caused by the pre-mixing of water and water-glucose solution prior to the begging of the experiment. That means, the initial condition on the experiment is slightly different to that used in the simulation. Nevertheless, the agreement between both methods is very good. The use of the Richardson number could also correctly predict the flow regime for this experiment.

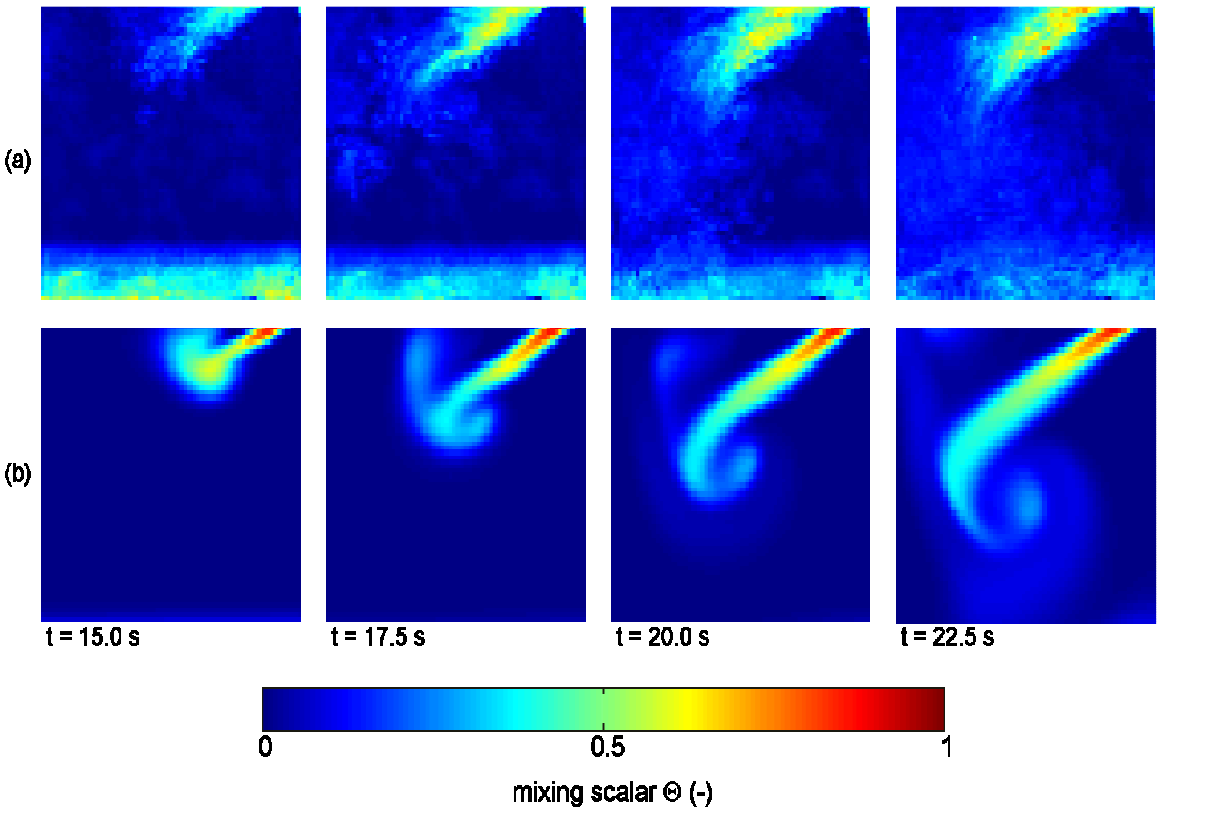

Fig. 6: Distributions of mixing scalar at the surface of VeMix test facility for the mixing experiment for Ri = 0.882: (a) planar array sensor measurement, (b) simulation with ANSYS CFX. For conditions see text.

4.2. Velocity fields

Further analysis of the measured data was carried out regarding computation of velocity field distribution. Fig. 7 illustrates four selected images of measured and the simulated velocity fields. The magnitude of the velocity is shown in terms of a color scale in the background and the velocity vectors are shown in the foreground.

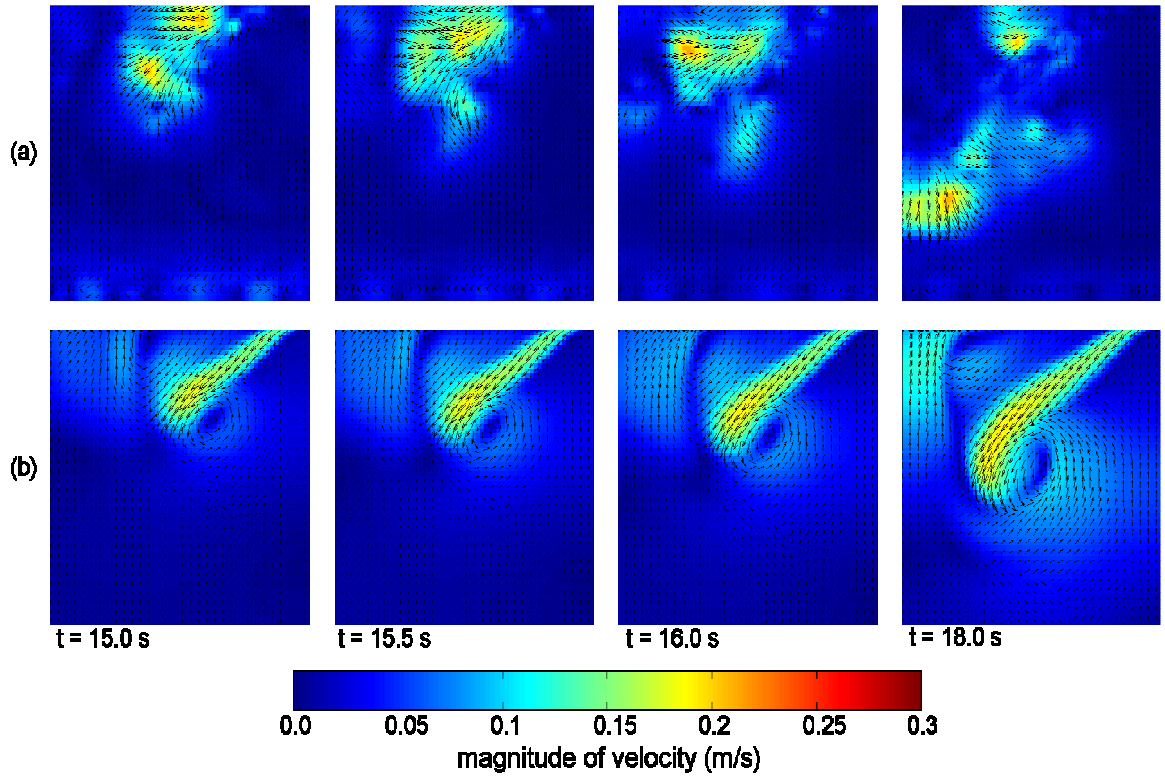

Fig. 7: Velocity fields at the surface of VeMix test facility for the mixing experiment for $Ri = 0.882$: (a) planar array sensor measurement and optical flow method, (b) simulation with ANSYS CFX. For conditions see text.

The simulation images show a very clear vortex at the bottom of the jet which bends the initial straight jet and creates the circular liquid distribution as observed in fig. 6. In the velocity field from the measured data the vortex is not perfectly clear, but still visible. Although the velocity field distributions cannot be said to be directly comparable, the main behavior can be extracted from the measurement and the agreement in the values of the magnitude is good, thus being a valuable qualitative validation for the simulation. Of course, for the quantitative comparisons purposes, the velocity measurement method must be better evaluated.

The image at $t = 18$ s is a good example for the limitation of the optical method. Due to the increasing mixing of the substances, the grayscale gradients become smaller and the algorithm accuracy tends to lower. The jet cannot be visualized in this image, but a velocity spot appears which is unphysical. The spot occurs because the gradient at that region was high. In spite of this limitation, the optical flow method is still able to evaluate the velocity field assuming the gradients in the grayscale are present. For the VeMix experiment described here, this occurs predominantly in the jet region and at the beginning of the experiment.

5. CONCLUSIONS

The VeMix test facility was constructed to investigate buoyancy driven flow which are relevant to nuclear safety scenarios. In the facility, the mixing of weakly and highly borated coolant can be investigated. The use of a new developed planar array sensor allows the measurement of the mixing scalar which can be directly and quantitatively compared with density distributions predicted from CFD simulations. In this paper, we also introduce a new method to assess velocity fields based on the planar sensor's measurements and the optical flow method. The preliminary results illustrated here show good agreement between experiments and simulations. Other experiments will be carried out in the VeMix test facility to further validate the CFD predictions, including quantitative comparisons. Further work regarding the velocity measurement may encompass the validation of optical flow method through simultaneous measurement with some other velocimetry method such as PIV, LDA. Furthermore, the limitations of the method should be better investigated.

ACKNOWLEGMENTS

This work was in part supported by the German Federal Ministry of Economy and Labor, grant 150 1287. M.J. Da Silva acknowledges the Brazilian agency CAPES for the financial support by a doctoral grant.

REFERENCES

S. S. Beauchemin, J. L. Barron "The Computation of Optical Flow" *University of Western Ontario*, (1995).

CFX11, *User Manual*, ANSYS-CFX (2007).

T. Corpetti, D. Heitz, G. Arroyol, É. Mémin, A. Santa-Cruz "Estimation of motion using a PIV correlation-based method and an "optical-flow" one for two experimental flows: quantitative and qualitative comparison" *12th International Symposium on Applications of Laser Techniques to Fluid Mechanics*, Lisbon, Portugal, (2004).

M.J. Da Silva, T. Sühnel, E. Schleicher, D. Lucas, R. Vaibar, U. Hampel, "Planar array sensor for high-speed component distribution imaging in fluid flow applications" *Sensors* 7, 2430-2445 (2007).

T. Höhne, S. Kliem, U. Bieder, "Modeling of a buoyancy-driven flow experiment at the ROCOM test facility using the CFD-codes CFX-5 and TRIO_U" *Nuclear Engineering and Design* 236, pp. 1309-1325 (2006)

B.K.P Horn, B.G. Schunck "Determining Optical Flow" *Artificial Intelligence* 17, 185-203 (1981).

B. Jähne *Digital Image Processing*, 5th revised and extended Edition, Springer, 2002.

F.R. Menter, "Zonal two equation k-ω turbulence models for aerodynamic flows". *Proc. of 24th AIAA Fluid Dynamics Conference*. Orlando, FL, AIAA paper 93-2906, July (1993).

U. Rohde, S. Kliem, T. Höhne, R. Karlsson, B. Hemström, J. Lillington, T. Toppila, J. Elter, Y. Bezrukov "Fluid mixing and flow distribution in the reactor circuit, measurement data base." *Nuclear Engineering and Design* 235, 421-443 (2005).

E.P. Simoncelli "Design of Multi-Dimensional Derivative Filters" *Proc. of 1st IEEE International Conference on Image Processing*, Austin, Texas, USA, 790-793 (1994).

S. Thiele *Entwicklung und Aufbau eines kapazitiven Oberflächensensors für die Phasenverteilung- und Geschwindigkeitsmessung zweiphasiger Strömungen*. Diploma Thesis, Technische Universität Dresden, Dresden, Germany (2007). *in german*.